NANO LETTERS
Letter
pubs.acs.org/NanoLett

High-Resolution Tracking Asymmetric Lithium Insertion and Extraction and Local Structure Ordering in SnS_2

Peng Gao,[*,†,‡] Liping Wang,[§] Yu-Yang Zhang,[*,∥] Yuan Huang,[⊥] Lei Liao,[#] Peter Sutter,[▽] Kaihui Liu,[‡,●] Dapeng Yu,[‡,●] and En-Ge Wang[‡,△]

[†] Electron Microscopy Laboratory, School of Physics, Peking University, Beijing 100871, China
[‡] Collaborative Innovation Center of Quantum Matter, Beijing 100871, China
[§] State Key Laboratory of Electronic Thin Films and Integrated Devices, University of Electronic Science and Technology of China, Chengdu 610054, China
[∥] Institute of Physics, Chinese Academy of Sciences, Beijing 100190, China
[⊥] Brookhaven National Laboratory, Upton, New York 11973, United States
[#] Department of Physics and Key Laboratory of Artificial Micro- and Nano-structures of Ministry of Education, Wuhan University, Wuhan 430072, China
[▽] Department of Electrical and Computer Engineering, University of Nebraska-Lincoln, Lincoln, Nebraska 68588, United States
[●] State Key Laboratory for Mesoscopic Physics, School of Physics, Peking University, Beijing 100871, China
[△] International Center for Quantum Materials, School of Physics, Peking University, Beijing 100871, China

Supporting Information

ABSTRACT: In the rechargeable lithium ion batteries, the rate capability and energy efficiency are largely governed by the lithium ion transport dynamics and phase transition pathways in electrodes. Real-time and atomic-scale tracking of fully reversible lithium insertion and extraction processes in electrodes, which would ultimately lead to mechanistic understanding of how the electrodes function and why they fail, is highly desirable but very challenging. Here, we track lithium insertion and extraction in the van der Waals interactions dominated SnS_2 by in situ high-resolution TEM method. We find that the lithium insertion occurs via a fast two-phase reaction to form expanded and defective $LiSnS_2$, while the lithium extraction initially involves heterogeneous nucleation of intermediate superstructure $Li_{0.5}SnS_2$ domains with a 1−4 nm size. Density functional theory calculations indicate that the $Li_{0.5}SnS_2$ is kinetically favored and structurally stable. The asymmetric reaction pathways may supply enlightening insights into the mechanistic understanding of the underlying electrochemistry in the layered electrode materials and also suggest possible alternatives to the accepted explanation of the origins of voltage hysteresis in the intercalation electrode materials.

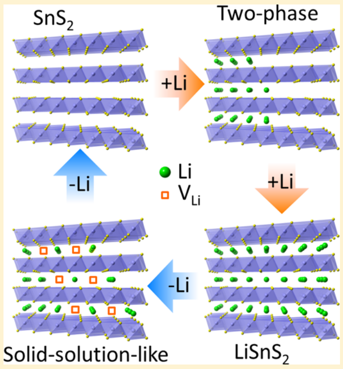

KEYWORDS: *Lithium ion battery, in situ TEM, first-principles calculation, intermediate phase, electrochemistry dynamics*

There has been great interest in probing the lithium ion transport dynamics and phase transition pathways in the electrodes of rechargeable lithium ion batteries (LIBs) in the hope of gaining a mechanistic understanding to guide optimization of the electrode materials.[1−10] A pervasive concern on the phase transition during Li insertion and extraction in the intercalation type of electrodes [e.g., $LiFePO_4$ (ref 11), $LiCoO_2$ (ref 12), $LiMn_2O_4$ (ref 13)] is whether Li ions transport occurs via solid-solution reactions or two-phase reactions.[1−3] The solid-solution reaction involving neither substantial structural rearrangements nor large volume changes underpins the high-rate capability of battery electrode materials,[1,2,12−14] whereas for the two-phase reaction additional kinetic barriers to the nucleation and growth of the second phase need to be overcome.[3] The equilibrium phase diagram, however, might be insufficient to predict the practical reaction pathways in some electrode materials. For example, the recent findings of metastable solid-solution phases in Li_xFePO_4 (refs2, 3, 10, 15) and of a $Li_{0.5}FePO_4$ lithium-staging phase[3,15,16] are in contradiction with its traditional two-phase model.

To better understand the dynamics of the phase transition, real-time tracking of lithium migration in electrodes therefore is required. The commonly used in situ X-ray diffraction,[2] absorption spectroscopy,[17] and nuclear magnetic resonance (NMR)[18] techniques can give valuable insights into the structure and chemistry of the electrode materials during the phase transition, while the recent advancement of in situ

Received: May 27, 2016
Revised: July 26, 2016
Published: August 9, 2016

DOI: 10.1021/acs.nanolett.6b02136
Nano Lett. 2016, 16, 5582−5588

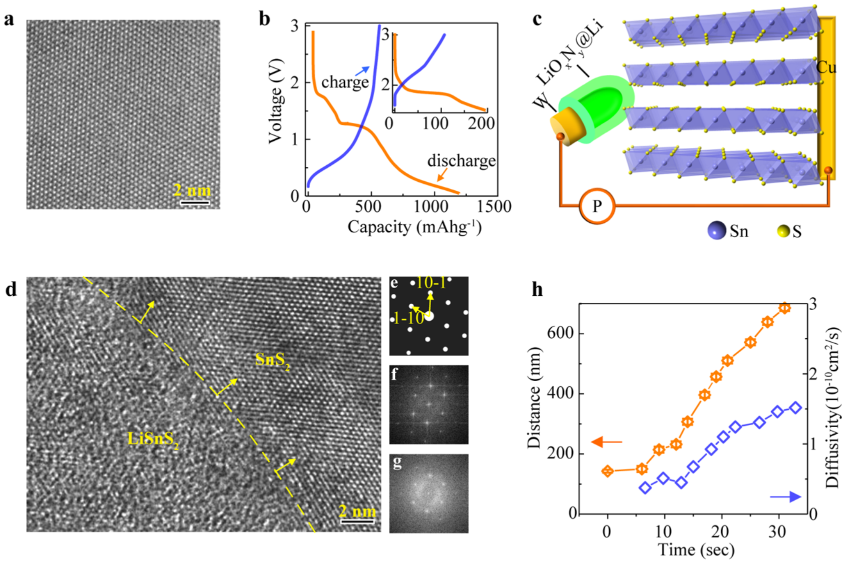

Figure 1. Tracking lithium ion transport in SnS_2 nanosheets in real time. (a) High-resolution transmission electron microscopy (TEM) image of SnS_2 nanosheets seen along [001] direction. (b) Galvanostatic charge/discharge curves of a carbon-SnS_2 composite versus a metallic lithium electrode between 3 and 0 V. Inset: intercalation−deintercalation curves between from 3 and 1.5 V. (c) Atomistic model of a SnS_2 nanosheet seen from the [010] direction. Sn atoms are octahedrally coordinated. Schematic also shows the Li-SnS_2 battery cell used for in situ TEM measurements consisting of a SnS_2 nanosheet, a metallic lithium probe, and a thin passivation layer of LiO_xN_y acting as solid-state electrolyte. (d) Upon lithium insertion, a high-resolution TEM image of a phase boundary between intercalated ($LiSnS_2$) and pristine (SnS_2) domains with viewing direction of [111]. The yellow dashed line highlights the reaction front (phase boundary). The arrows indicate the reaction front motion direction. (e) Simulated electron diffraction pattern of single crystal SnS_2 viewing along [111] direction. (f) FFT pattern from the right corner of pristine SnS_2 domain. (g) FFT pattern from the left corner of the intercalated domain $LiSnS_2$ is diffuse and less intense. After lithium intercalation, the measured lattice expansion from FFT is ~4.3−4.5%. (h) Distance of the reaction front propagation and diffusivity are plotted as functions of time calculated from Movie S1. The error bars come from the uncertainties in defining the boundaries (~10−30 nm).

transmission electron microscopy (TEM) has higher spatial and temporal resolutions to probe the phase nucleation and phase boundary propagation in battery systems[6−10,19−21] and track the localized and/or intermediate phases that might only have existed within a short time scale.

Here, we use an in situ high-resolution TEM (HRTEM) technique to track the reversible phase transitions during Li ions insertion and extraction in SnS_2 nanostructures which have large theoretical capacities for lithium and sodium ion batteries.[22−30] In SnS_2 (JCPDS Card No. 01-1010), the adjacent sulfur layers are bonded by the weak van der Waals interactions. For these layered metal dichalcogenide structures, previous studies of TiS_2 from first-principles calculations[31,32] and NMR[33,34] indicated that the behaviors of alkali ions migration are very different than those in the covalent or ionic transition metal oxides with variable valences.

We find that the Li insertion occurs via a fast two-phase reaction initiated by nucleation of a new phase, $LiSnS_2$, with expanded lattice and richness of defects and followed by propagation of the phase boundary. The Li extraction, however, involves intermediate phases with local structure ordering (i.e., $Li_{0.5}SnS_2$) instead of retracting the original phase boundary. These $Li_{0.5}SnS_2$ domains with size of ~1−4 nm nucleate rapidly and heterogeneously upon lithium extraction, followed by domain merging and shrinking. Our study shows that the reaction pathways during Li ion insertion and extraction can be significantly different even in the intercalation range of SnS_2, which is in contrast to (and in contradiction with) the general two-phase reaction mode. In addition, the atomic structure and dynamic evolutions of the intermediate superstructure ($Li_{0.5}SnS_2$) have been determined. Combining with density functional theory (DFT) calculations, we conclude that this intermediate phase with local structure ordering in the layered structure is kinetically favored and structurally stable. The findings of distinct lithium insertion and extraction reaction pathways provide valuable insights into the mechanistic understanding of the underlying electrochemistry in the van der Waals interactions electrode materials and may also help to elucidate the origins of voltage hysteresis in intercalation electrodes and thus design high-energy efficiency batteries.

Results. *Two-Phase Reaction during Lithium Insertion.* Typical electrochemical measurements of Li anode and SnS_2 cathode battery cells were performed and shown in Figure 1a and b. The lithium intercalation that corresponds to the plateau of the curve in the inset of Figure 1b delivers a capacity ~144 mA·h/g, indicating that each SnS_2 unit can intercalate 0−0.98 Li (Li_xSnS_2, $x \sim 1$ will be discussed below). To real-time track the structural evolution during lithium migration in SnS_2, in situ TEM experiments[7−10,21] were carried out (in Figure 1c, see Methods section for details). Upon Li intercalation, a phase boundary between SnS_2 and $LiSnS_2$ domains is clearly shown in Figure 1d. The two-phase reaction mode is further confirmed by the electron diffraction pattern in Figure S1. After lithium insertion, the lattice of $LiSnS_2$ becomes disordered in Figure 1d. The fast Fourier transform (FFT) pattern from the $LiSnS_2$ domain (Figure 1g) shows a similar pattern but more diffuse and less intense spots compared to the pristine state (Figure 1f), indicating that after Li intercalation the structural framework still remains but becomes defective. Indeed, the HRTEM images in Figure S2 confirm that the well-stacked layer structure of the pristine state has been broken into small segments with defects after lithium insertion and the edge dislocations and antiphase boundaries are identified from the filtered image of $LiSnS_2$ phase. The lattice expansion induced

DOI: 10.1021/acs.nanolett.6b02136
Nano Lett. 2016, 16, 5582−5588

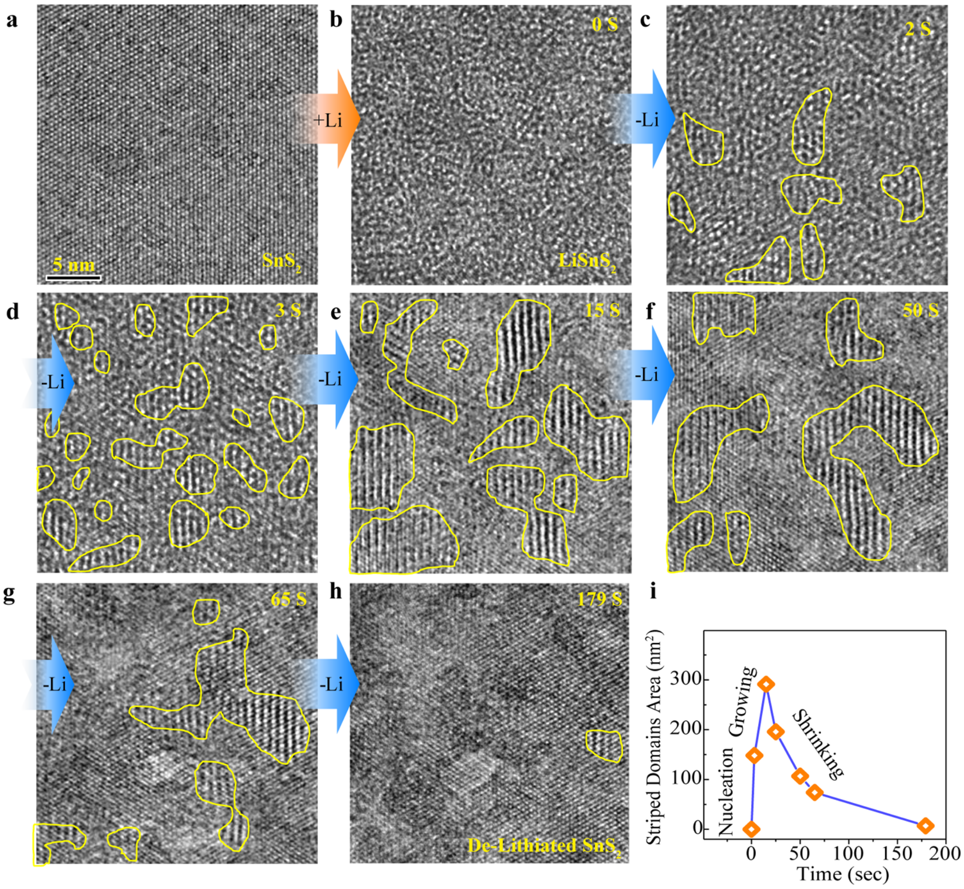

Figure 2. High-resolution transmission electron microscopy tracking of the intermediate superstructure evolution during Li extraction. (a) Pristine state SnS_2. The TEM image is recorded from [111] direction. (b) The same region of lithium intercalated state $LiSnS_2$. The process of lithium insertion is too fast to capture in high-resolution mode in Movies S2. (c–h) Structural evolution during Li extraction (see also Movie S3). The yellow outlines highlight the striped superstructure domains. The striped domains nucleate quickly and heterogeneously. (h) After ~179 s, most of striped superstructure domains have disappeared. The lattice is recovered similar to the pristine state. (i) The total striped domain area is plotted as a function of time from the selected region.

by Li insertion is measured to be ~4.5% in [100] direction (in Figure 1f,g and Figure S1) and ~4.6% along the [001] direction, which is also reproduced by the first-principles calculations of ~3.5% and ~4.9% expansion in the *a*-direction and *c*-direction (see Table S1), respectively. With further lithiation, the saturated Li_xSnS_2 phase converts very quickly into Li_2S and Sn within a few seconds (<7 s), followed by the formation of Li_ySn alloy ($y \sim 4.4$) in Figure S3.

The velocity of the phase boundary motion (in Movie S1 and Figure S4) is calculated to be ~10–40 nm/s in Figure S5, which can be approximately equivalent to a discharge rate of 116 C in a realistic battery with proper engineering. The diffusivity is estimated to be ~$0.3-1.5 \times 10^{-10}$ cm²/s in Figure 1h based on the equation $D = d^2/t$, where D is diffusivity, d is the diffusion distance, and t is the diffusion time.

Intermediate Superstructure during Lithium Extraction. Once the lithiation in SnS_2 is controlled within the range of intercalation (see Movie S2), the lithium ions in $LiSnS_2$ can be completely extracted as shown in Figure 2 (see also Figure S6 and Movie S3). Compared to the fast lithium insertion process (Figure 2a–b), Li extraction (in Figure 2b–h) is much slower. At the beginning of lithium extraction, a few small domains with a size of ~1–4 nm (measured in Figure S7) appear and gradually grow. The small domains show local structural ordering as highlighted by the yellow outlines in Figure 2c–h. These striped domains then merge together (Figure 2e) and slowly shrink in size with further Li extraction (from Figure 2e to h). The total area and counts of striped domains in this selected region is plotted as a function of time in Figure 2i and Figure S7, respectively, confirming that the striped domains grow quickly and die away slowly. Furthermore, the phase transformation is fully reversible under the electron beam illumination in Figure 2, indicating the observed phase transition is induced by lithium insertion/extraction instead of the electron beam irradiation effect.

Structure of Intermediate Superstructure. The structure with local structural ordering is further determined by HRTEM images and their FFT patterns in Figure 3. The FFT patterns of HRTEM images recorded during lithium extraction in Figure 3a show extra superstructure spots {1/2 0 1/2}. The distance of stripes in the filtered HRTEM image in Figure 3b is measured to be twice the distance of {101} planes of the SnS_2. An atomic model therefore can be reconstructed in Figure 3c. Along the [10–1] direction, in every two-unit cell only one interlayer is occupied by lithium, corresponding to $Li_{0.5}SnS_2$. Along the [010] viewing direction in Figure 3d, in each layer half of the lithium columns are removed. Although the superstructure cannot be captured by the electron diffraction due to the nature of localization and intermediate, the atomistic structure is confirmed by the electron diffraction simulation in Figure 3e.

DOI: 10.1021/acs.nanolett.6b02136
Nano Lett. 2016, 16, 5582–5588

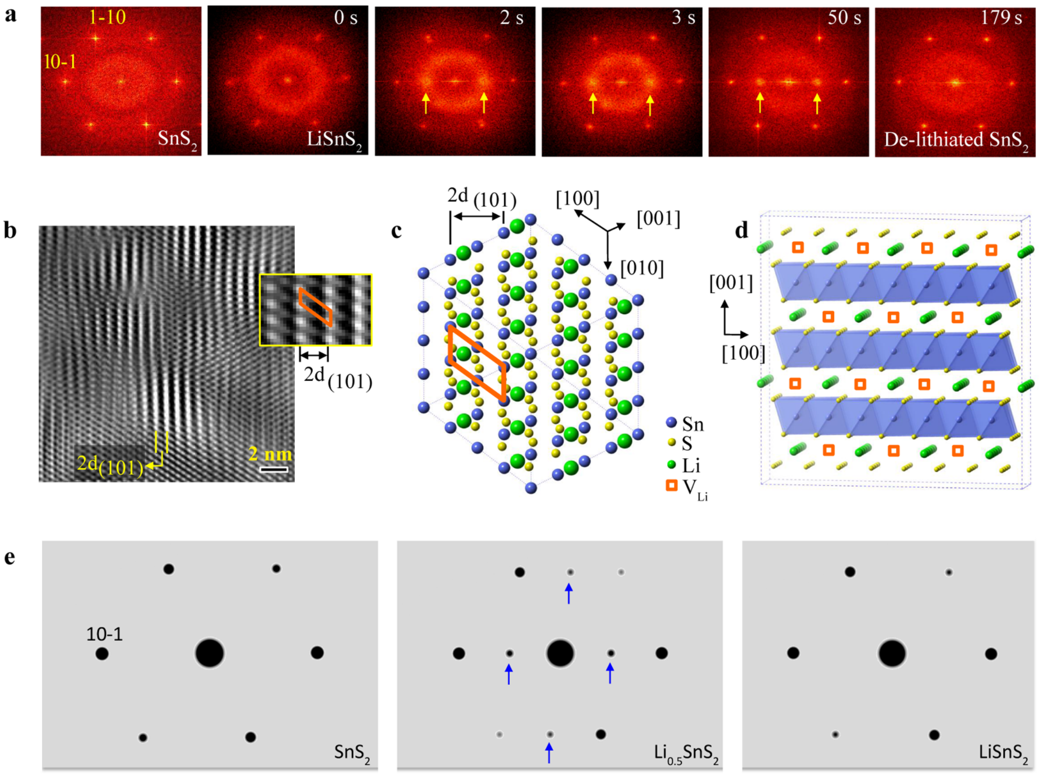

Figure 3. Atomic structure of the intermediate superstructure. (a) Selected FFT patterns of images shown in Figure 2. (b) Fourier space filtered image from striped domains. A unit cell of the superstructure is highlighted by solid orange lines in the right inset. The distance of lattice fringes in the striped domain is measured to be twice the distance of {101}-SnS$_2$ planes. (c) An atomic structure of striped domain seen from [111] direction based on the high-resolution TEM images and FFT patterns. Along [10−1] direction, in every two-unit cell only one is occupied by Li ions. A unit cell of superstructure is highlighted by solid orange outline. (d) The same structure with viewing direction along slightly tilted [010]. Along this viewing direction, in each layer half of the lithium columns are removed. (e) Left: the simulated electron diffraction pattern of Sn_8S_{16} (SnS$_2$). Middle: the simulated electron diffraction pattern of $Li_4Sn_8S_{16}$ (intermediate superstructure $Li_{0.5}SnS_2$). The blue arrows denote extra spots from the superstructure $Li_{0.5}SnS_2$. Right: The simulated electron diffraction pattern of $Li_8Sn_8S_{16}$ (LiSnS$_2$).

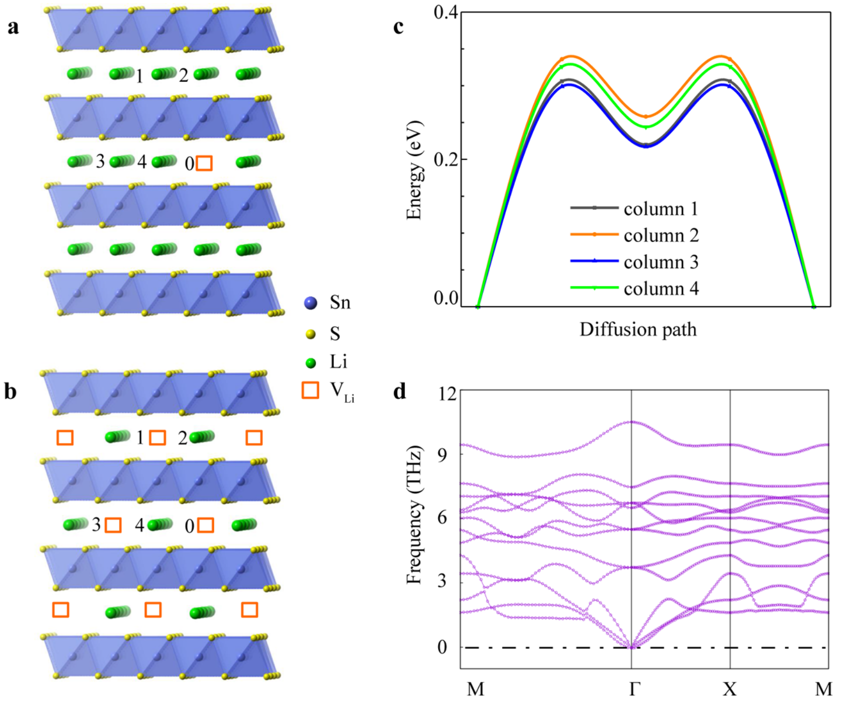

Figure 4. Formation process and stability of the lithium ordered intermediate superstructure. (a) Structure of $Li_{0.94}SnS_2$ with one pre-extracted lithium column (labeled 0). (b) Structure of the lithium ordered phase, i.e., $Li_{0.5}SnS_2$. (c) Energy profile of lithium diffusion process in different columns. (d) Phonon dispersion of the proposed $Li_{0.5}SnS_2$ structure.

First-Principles Calculations. First-principles calculations were carried out to understand the lithium transport process and the formation of the intermediate superstructure $Li_{0.5}SnS_2$. We first illustrate the fast lithium insertion and slow lithium extraction processes by comparing lithium migration barrier at dilute lithium/vacancy situation. The lithium deficient condition is considered for the Li insertion process in which one Li is inserted into 32 SnS_2 unites ($Li_{0.03}SnS_2$). In this case, the calculations indicate that the octahedrally sited Li migrates to the neighboring octahedron through a tetrahedral site as an intermediate state, i.e., $Li_{oct} \rightarrow Li_{tet} \rightarrow Li_{oct}$ (black arrow in Figure S8). The migration barrier is 0.29 eV. The existence of the intermediate site significantly lowers the activation energy.[31,32] At the initial stage of lithium extraction, the Li migration can be considered as the vacancy diffusion. One Li vacancy is created in 32 $LiSnS_2$ unites ($Li_{0.97}SnS_2$). The calculated energy barrier is 0.35 eV, resulting in a much slower lithium extraction process compared to the lithium insertion, which is in good agreement with the experimental observations.

To explore the formation of the intermediate superstructure with ordered lithium vacancies, $-Li_{0.5}SnS_2-$, different ways of lithium extraction were tested. We first assume that there is already a pre-extracted lithium column in $LiSnS_2$ (labeled as 0 in Figure 4a). Then we considered the next possible extraction site by comparing the energy with lithium extraction in different column (from column 1 to column 4). It is found that forming an extra lithium vacancy in column 1 and 3 is easier than that in column 2 and 4 by 0.07 eV. We also consider the kinetic process by comparing vacancy migration barrier in different columns. It is found that with the pre-extracted lithium column, vacancy migration barriers in column 1 and 3 (along [010] direction) are lower than those in column 2 and 4 by 0.05 eV, which approximately corresponds to a 10 times faster diffusion at room temperature. In other words, once there is a vacancy in column 1 or 3, the entire column will be removed quickly, resulting in the vacancy ordered structure (Figure 4b). The migration barrier in different column with pre-extracted lithium is shown in Figure 4c, and details of the calculations can be found in Supporting Information. We also investigate the structural stability of the vacancy ordered intermediate superstructure by checking the existence of negative-frequency phonon modes, which is a powerful tool to guide phase transition.[35] As shown in Figure 4d, there is no negative-frequency phonon mode, thus proving that the proposed $Li_{0.5}SnS_2$ structure with lithium vacancy ordering is stable.

Discussion. It is well-known that in LIBs the energy efficiency is determined by the voltage hysteresis between lithiation and delithiation, i.e., asymmetric reaction pathways usually lead to large voltage hysteresis and subsequent low energy efficiency. Although asymmetric reaction pathways between discharge and charge are frequently observed in conversion electrode materials,[36−38] alloying,[39,40] and displacement[41] reactions, for intercalation electrode materials symmetric reaction pathways are usually expected[5] from the equilibrium phase diagram, and the origin of the voltage hysteresis therefore is believed to be the fact that the particles do not react with lithium simultaneously.[5] However, our observations show that the lithium ion extraction in SnS_2 involves multiple phases and heterogeneous reactions, which is significantly different from the two-phase reaction during insertion (Figure S10), suggesting possible alternatives to the accepted explanation[5] of the origins of voltage hysteresis for intercalation electrode materials. In fact, such asymmetric reaction pathways are in good agreement with the asymmetric intercalation-deintercalation curves measured in the coin cells in Figure 1b where the intercalation process shows a plateau indicating a two-phase reaction behavior while the deintercalation process presents a sloped curve with solid solution-like behavior.[42,43]

Conclusion. In summary, we have tracked the phase transition during lithium ion insertion and extraction in the weak van der Waals interactions dominated SnS_2 nanostructures in real-time and with lattice fringe resolution. The SnS_2 adopts lithium ions between the sulfide layers to form an intercalated $LiSnS_2$ phase with expanded lattice and defects via a fast two-phase reaction. The lithium extraction reaction pathway is distinct from that of the lithium insertion. Upon lithium extraction, the $Li_{0.5}SnS_2$ domains with vacancies ordering nucleate quickly and heterogeneously, followed by domain merging, slow shrinking, and disappearance. Our direct observations reveal the dynamics and kinetics of lithium insertion and extraction in SnS_2 nanostructures. In particular, for the first time the atomic structure of intermediate lithium ordering phase $Li_{0.5}SnS_2$ has been identified, and the dynamic evolution behaviors have been captured in real-time. These observations can help us to understand the lithium diffusion mechanism in layered structures which are dominated by the van der Waals interactions. Furthermore, in such an intercalation electrode material the asymmetric reactions pathways, i.e., two-phase insertion reaction and solid solution-like extraction reaction that involves intermediate phases, suggest a new possible model for the origins of the voltage hysteresis for intercalation electrodes, providing valuable insights into improving the energy efficiency of lithium ion batteries.

Experimental Section. *Eletrochemical Measurements.* For the electrochemical measurements, the electrode was prepared by SnS_2 (80 wt %), carbon black (10 wt %), and polyvinylidene fluoride (10 wt %) in *N*-methylpyrrolidone to form a homogeneous slurry with then spread onto a copper foil and dried at 100 °C for an overnight in a vacuum oven. Lithium foil and polypropylene membrane (celgard 2400) were used as the anode and the separator, respectively. Commercial electrolyte LP30 (1 M LiPF6 in a mixture of ethylene carbonate, dimethyl carbonate (1:1 by volume)) was used as the electrolyte. 2032 coin cells were assembled in an argon-filled glovebox. The batteries were galvanostatic discharged and charged on a LAND CT2001A cell test apparatus at room temperature. The weight of our electrode materials is about 2.0 mg/cm^2.

TEM Experiments. The SnS_2 nanosheets with layered structure were mechanically peeled off from a single crystal by using a half TEM Cu grid to scratch the surface of SnS_2 crystal. The Cu grid acts as one current collector, and SnS_2 is considered to be working electrode. The typical thickness of SnS_2 nanosheet varies from a few nanometers to tens of nanometers. Lithium metal (acting as the counter electrode) was coated onto a sharp tungsten probe. All of the components were loaded onto a costumed TEM specimen holder (PicoFemto) integrated with electrical biasing probe in argon-filled glovebox and then transferred into the TEM column using argon-filled plastic bag. During transferring the holder into the TEM chamber, the lithium metal was intentionally exposed to air (~2 s) to form a thin passivation layer of LiN_xO_y on the surface that acted as solid-state electrolyte to allow transport of lithium ions. The lithium insertion was initiated by applying a small negative bias between the tungsten probe and the grounded Cu grid, while the lithium extraction was driven by a small positive bias.

Data Acquisition and Analysis. Both TEM images and electron diffraction patterns (ED) were recorded by a Gatan CCD. Movies are made by continuous images. The atomistic models were generated by Crystalmaker software. The plots were created by Origin 8.5. The FFT patterns and inverse FFT were calculated by DigitalMicrograph (Gatan) software. The domain area was calculated by ImageJ software. The simulation of electron diffraction was carried by commercial software SingleCrystal 2.3.3 for Mac system.

DFT Calculations. First-principles calculations are carried out based on density functional theory, projector augmented waves,[44] a restoring Perdew−Burke−Ernzerhof functional in solid and surface (PBEsol),[45] and a plane wave basis set which is implemented in the Vienna Ab initio Simulation Package.[46] We use a 520 eV energy cutoff as the plane-wave basis set, 0.01 eV/Å as the force criteria, and 10^{-5} eV as the energy convergence criteria. Lattice constants are optimized when stress in each direction is smaller than 0.05 GP. For pristine SnS_2, the calculated lattice constants in *a* and *c* direction are 3.65 and 6.09 Å, respectively, which are in satisfactory agreement with experimental values (3.65 and 5.90 Å).[47] Climbing nudged elastic band method[48] is used to calculate the diffusion barrier. A 4 × 4 × 2 supercell is used to model the beginning of lithium insertion and extraction process. Seven images were inserted between the initial and final configurations. A 4 × 4 × 4 supercell is used to model the formation of $Li_{0.5}SnS_2$. Three images were inserted between the initial and final configurations. *k*-point samplings in the Brillouin zone were fully tested to converge the energy to 1 meV/atom.

■ ASSOCIATED CONTENT

Supporting Information

The Supporting Information is available free of charge on the ACS Publications website at DOI: 10.1021/acs.nanolett.6b02136.

Lithium insertion via a two-phase reaction, lithium intercalation induced defects seen perpendicular to [001] direction, conversion and alloying reactions, tracking the phase boundary between SnS_2 and $LiSnS_2$, reaction front propagation during lithium insertion in SnS_2, structural evolution during reversible lithium insertion and extraction, the area of striped domain during lithium extraction, lithium diffusion at the beginning of charge and discharge process, an example of vacancy migration to form the intermediate superstructure, asymmetric reactions pathways during lithium insertion and extraction, and calculated atomic configuration of SnS_2 and $LiSnS_2$ (PDF)

Lithium insertion in SnS_2 nanostructures recorded at low magnification (AVI)

Lithium insertion in SnS_2 nanostructures recorded at high resolution (AVI)

Lithium extraction and intermediate structure ordering evolution (AVI)

■ AUTHOR INFORMATION

Corresponding Authors

*E-mail: p-gao@pku.edu.cn.
*E-mail: yyzhang@iphy.ac.cn.

Notes

The authors declare no competing financial interest.

■ ACKNOWLEDGMENTS

This work was supported by the National Natural Science Foundation of China (51502007, 51502032, 51522201), National Basic Research Program of China (2016YFA0300903), the National Program for Thousand Young Talents of China, and "2011 Program" Peking-Tsinghua-IOP Collaborative Innovation Center of Quantum Matter. Computational resources (Y.Y.Z.) were provided by the Extreme Science and Engineering Discovery Environment (XSEDE), which is supported by National Science Foundation grant number ACI-1053575.

■ REFERENCES

(1) Kang, B.; Ceder, G. *Nature* **2009**, *458*, 190−193.

(2) Liu, H.; Strobridge, F. C.; Borkiewicz, O. J.; Wiaderek, K. M.; Chapman, K. W.; Chupas, P. J.; Grey, C. P. *Science* **2014**, *344*, 1252817.

(3) Malik, R.; Zhou, F.; Ceder, G. *Nat. Mater.* **2011**, *10*, 587−590.

(4) Delmas, C.; Maccario, M.; Croguennec, L.; Le Cras, F.; Weill, F. *Nat. Mater.* **2008**, *7*, 665−671.

(5) Dreyer, W.; Jamnik, J.; Guhlke, C.; Huth, R.; Moskon, J.; Gaberscek, M. *Nat. Mater.* **2010**, *9*, 448−453.

(6) Huang, J. Y.; Zhong, L.; Wang, C. M.; Sullivan, J. P.; Xu, W.; Zhang, L. Q.; Mao, S. X.; Hudak, N. S.; Liu, X. H.; Subramanian, A.; et al. *Science* **2010**, *330*, 1515−1520.

(7) Liu, X. H.; Wang, J. W.; Huang, S.; Fan, F.; Huang, X.; Liu, Y.; Krylyuk, S.; Yoo, J.; Dayeh, S. A.; Davydov, A. V.; et al. *Nat. Nanotechnol.* **2012**, *7*, 749−756.

(8) Zhu, Y.; Wang, J. W.; Liu, Y.; Liu, X.; Kushima, A.; Liu, Y.; Xu, Y.; Mao, S. X.; Li, J.; Wang, C.; et al. *Adv. Mater.* **2013**, *25*, 5461−5466.

(9) Wang, L.; Xu, Z.; Wang, W.; Bai, X. *J. Am. Chem. Soc.* **2014**, *136*, 6693−6697.

(10) Niu, J.; Kushima, A.; Qian, X.; Qi, L.; Xiang, K.; Chiang, Y.-M.; Li, J. *Nano Lett.* **2014**, *14*, 4005−4010.

(11) Padhi, A. K.; Nanjundaswamy, K. S.; Goodenough, J. B. *J. Electrochem. Soc.* **1997**, *144*, 1188−1194.

(12) Reimers, J. N.; Dahn, J. R. *J. Electrochem. Soc.* **1992**, *139*, 2091−2097.

(13) Thackeray, M. M.; Johnson, P. J.; Depicciotto, L. A.; Bruce, P. G.; Goodenough, J. B. *Mater. Res. Bull.* **1984**, *19*, 179−187.

(14) Ohzuku, T.; Makimura, Y. *Chem. Lett.* **2001**, *30*, 642−643.

(15) Sun, Y.; Lu, X.; Xiao, R.; Li, H.; Huang, X. *Chem. Mater.* **2012**, *24*, 4693−4703.

(16) Gu, L.; Zhu, C.; Li, H.; Yu, Y.; Li, C.; Tsukimoto, S.; Maier, J.; Ikuhara, Y. *J. Am. Chem. Soc.* **2011**, *133*, 4661−4663.

(17) Yu, X.; Lyu, Y.; Gu, L.; Wu, H.; Bak, S.-M.; Zhou, Y.; Amine, K.; Ehrlich, S. N.; Li, H.; Nam, K.-W.; et al. *Adv. Energy Mater.* **2014**, *4*, 1300950.

(18) Hu, Y.-Y.; Liu, Z.; Nam, K.-W.; Borkiewicz, O. J.; Cheng, J.; Hua, X.; Dunstan, M. T.; Yu, X.; Wiaderek, K. M.; Du, L.-S.; et al. *Nat. Mater.* **2013**, *12*, 1130−1136.

(19) Luo, L.; Wu, J.; Xu, J.; Dravid, V. P. *ACS Nano* **2014**, *8*, 11560−11566.

(20) He, K.; Xin, H. L.; Zhao, K.; Yu, X.; Nordlund, D.; Weng, T.-C.; Li, J.; Jiang, Y.; Cadigan, C. A.; Richards, R. M.; et al. *Nano Lett.* **2015**, *15*, 1437−1444.

(21) Gao, P.; Wang, L. P.; Zhang, Y. Y.; Huang, Y.; Liu, K. H. *ACS Nano* **2015**, *9*, 11296−11301.

(22) Morales, J.; Perezvicente, C.; Tirado, J. L. *Solid State Ionics* **1992**, *51*, 133−138.

(23) Brousse, T.; Lee, S. M.; Pasquereau, L.; Defives, D.; Schleich, D. M. *Solid State Ionics* **1998**, *113*, 51−56.

(24) Li, H.; Huang, X. J.; Chen, L. Q. *Solid State Ionics* **1999**, *123*, 189−197.

(25) Lefebvre-Devos, I.; Olivier-Fourcade, J.; Jumas, J. C.; Lavela, P. *Phys. Rev. B: Condens. Matter Mater. Phys.* **2000**, *61*, 3110−3116.

(26) Julien, C.; PerezVicente, C. *Solid State Ionics* **1996**, *89*, 337−343.

(27) Momma, T.; Shiraishi, N.; Yoshizawa, A.; Osaka, T.; Gedanken, A.; Zhu, J. J.; Sominski, L. *J. Power Sources* **2001**, *97*−*98*, 198−200.

(28) Kim, T. J.; Kim, C.; Son, D.; Choi, M.; Park, B. *J. Power Sources* **2007**, *167*, 529−535.

(29) Seo, J.-W.; Jang, J.-t.; Park, S.-W.; Kim, C.; Park, B.; Cheon, J. *Adv. Mater.* **2008**, *20*, 4269−4273.

(30) Qu, B.; Ma, C.; Ji, G.; Xu, C.; Xu, J.; Meng, Y. S.; Wang, T.; Lee, J. Y. *Adv. Mater.* **2014**, *26*, 3854−3859.

(31) Van der Ven, A.; Thomas, J. C.; Xu, Q.; Swoboda, B.; Morgan, D. *Phys. Rev. B: Condens. Matter Mater. Phys.* **2008**, *78*, 104306.

(32) Van der Ven, A.; Bhattacharya, J.; Belak, A. A. *Acc. Chem. Res.* **2013**, *46*, 1216−1225.

(33) Wilkening, M.; Kuchler, W.; Heitjans, P. *Phys. Rev. Lett.* **2006**, *97*, 065901.

(34) Wilkening, M.; Heitjans, P. *Phys. Rev. B: Condens. Matter Mater. Phys.* **2008**, *77*, 024311.

(35) Sternik, M.; Parlinski, K. *J. Chem. Phys.* **2005**, *122*, 064707.

(36) Ko, J. K.; Wiaderek, K. M.; Pereira, N.; Kinnibrugh, T. L.; Kim, J. R.; Chupas, P. J.; Chapman, K. W.; Amatucci, G. G. *ACS Appl. Mater. Interfaces* **2014**, *6*, 10858−10869.

(37) Boesenberg, U.; Marcus, M. A.; Shukla, A. K.; Yi, T.; McDermott, E.; Teh, P. F.; Srinivasan, M.; Moewes, A.; Cabana, J. *Sci. Rep.* **2014**, *4*, 7133.

(38) Doe, R. E.; Persson, K. A.; Meng, Y. S.; Ceder, G. *Chem. Mater.* **2008**, *20*, 5274−5283.

(39) Chang, D.; Huo, H.; Johnston, K. E.; Ménétrier, M.; Monconduit, L.; Grey, C. P.; Van der Ven, A. *J. Mater. Chem. A* **2015**, *3*, 18928−18943.

(40) Key, B.; Morcrette, M.; Tarascon, J.-M.; Grey, C. P. *J. Am. Chem. Soc.* **2011**, *133*, 503−512.

(41) Yu, H. C.; Ling, C.; Bhattacharya, J.; Thomas, J. C.; Thornton, K.; Van der Ven, A. *Energy Environ. Sci.* **2014**, *7*, 1760.

(42) Wang, L. P.; Li, H.; Huang, X. J.; Baudrin, E. *Solid State Ionics* **2011**, *193*, 32−38.

(43) Zaghib, K.; Guerfi, A.; Hovington, P.; Vijh, A.; Trudeau, M.; Mauger, A.; Goodenough, J. B.; Julien, C. M. *J. Power Sources* **2013**, *232*, 0378−7753.

(44) Blochl, P. E. *Phys. Rev. B: Condens. Matter Mater. Phys.* **1994**, *50*, 17953−17979.

(45) Perdew, J. P.; Ruzsinszky, A.; Csonka, G. I.; Vydrov, O. A.; Scuseria, G. E.; Constantin, L. A.; Zhou, X.; Burke, K. *Phys. Rev. Lett.* **2008**, *100*, 136406.

(46) Kresse, G.; Furthmuller, J. *Comput. Mater. Sci.* **1996**, *6*, 15−50.

(47) Hazen, R. M.; Finger, L. W. *Am. Mineral.* **1978**, *63*, 289−292.

(48) Henkelman, G.; Uberuaga, B. P.; Jonsson, H. *J. Chem. Phys.* **2000**, *113*, 9901−9904.